Nano Energy 65 (2019) 104035

Contents lists available at ScienceDirect

Nano Energy

journal homepage: www.elsevier.com/locate/nanoen

Full paper

Versatile neuromorphic electronics by modulating synaptic decay of single organic synaptic transistor: From artificial neural networks to neuro-prosthetics

Dae-Gyo Seo[a,1], Yeongjun Lee[a,1], Gyeong-Tak Go[a], Mingyuan Pei[b], Sungwoo Jung[c], Yo Han Jeong[d], Wanhee Lee[e], Hea-Lim Park[a], Sang-Woo Kim[d], Hoichang Yang[b], Changduk Yang[c], Tae-Woo Lee[a,f,*]

[a] Department of Materials Science and Engineering, Seoul National University (SNU), Seoul, Republic of Korea
[b] Department of Chemical Engineering, Inha University, Incheon, 22212, Republic of Korea
[c] Department of Energy Engineering, School of Energy and Chemical Engineering, Perovtronics Research Center, Low Dimensional Carbon Materials Center, Ulsan National Institute of Science and Technology (UNIST), Ulsan, Republic of Korea
[d] School of Advanced Materials Science & Engineering, Sungkyunkwan University (SKKU), Suwon, Gyeonggi-do, Republic of Korea
[e] Department of Physics and Astronomy, Seoul National University (SNU), Seoul, Republic of Korea
[f] Institute of Engineering Research, Research Institute of Advanced Materials, BK21 PLUS SNU Materials Division for Educating Creative Global Leaders, Seoul National University (SNU), Seoul, Republic of Korea

ARTICLE INFO

Keywords:
Neuromorphic electronics
Artificial synapses
Neuromorphic computing
Artificial auditory systems
Artificial nerves

ABSTRACT

Organic neuromorphic electronics are inspired by a biological nervous system. Bio-inspired computing mimics learning and memory in a brain (i.e., the central nervous system), and bio-inspired soft robotics and nervous prosthetics mimics the neural signal transmission of afferent/efferent nerves (i.e., the peripheral nervous system). Synaptic decay time of nerves differ among biological organs, so the decay time of artificial synapses should be tuned for their specific uses in neuro-inspired electronics. However, controlling a synaptic decay constant in a fixed synaptic device geometry for broad applications was not been achieved in previous research of neuromorphic electronic devices despite the importance to achieve broad applications from neuromorphic computing to neuro-prosthetics. Here, we tailored the synaptic decay constant of organic synaptic transistors with fixed materials and devices structure rather than changing the form of presynaptic spikes, which enabled broad applications from neuromorphic computing to neuro-prosthetics. To achieve this, the relation between crystallinity of the polymer semiconductor film and the synaptic decay constant was revealed. The crystallinity of the polymer controlled electrochemical-doping kinetics and resultant synaptic behaviors of artificial synaptic transistors. In this way, we demonstrated not only long-term retention for learning and memory that is useful for neuromorphic computing in ion-gel gated organic synaptic transistor (IGOST) but also the short-term retention for fast synaptic transmission that is useful for emulating peripheral nerves such as sensory and motor nerve. To prove the feasibility of our approach in a two different ways, we first simulated pattern recognition on the MNIST dataset of handwritten digits using an IGOST with long-term retention due to increased crystallinity and then, developed artificial auditory sensory nerves that combines an IGOST with short term retention due to disordered chain morphology in a polymer semiconductor, with a triboelectric acoustic sensor. We expect that our approach will provide a universal strategy to realize wide neuromorphic electronic applications.

1. Introduction

A biological nervous system is an extremely compact and well–organized collection of a large number of neurons and synapses [1,2]. Neural signals (i.e., action potentials) are transmitted through the neurons and synapses, which result in learning and memory in the brain (i.e., central nerves) or sensing and action in the body (i.e., peripheral nerves). Biological synapses have different decay-time constants

* Corresponding author. Department of Materials Science and Engineering, Seoul National University (SNU), Seoul, Republic of Korea.
E-mail addresses: twlees@snu.ac.kr, taewlees@gmail.com (T.-W. Lee).
[1] These authors equally contributed to this work.

https://doi.org/10.1016/j.nanoen.2019.104035
Received 25 June 2019; Received in revised form 6 August 2019; Accepted 16 August 2019
Available online 19 August 2019
2211-2855/

depending on their roles and locations [3–6]. Emulating the various decay time of synapses may be an important step toward developing various neuromorphic devices that mimic different nerves in central and peripheral nervous systems.

Development of neuromorphic devices has mostly focused on mimicking learning and memory of a biological brain [7–9]. On the other hand, organic neuromorphic electronics for brain-inspired computing and bio-inspired soft robotics can emulate both rules of neural signal transmission and neuroplasticity in a brain and peripheral nervous system [7,10–15]. Furthermore, organic synaptic transistors have advantages of low-cost solution fabrication, low-voltage-driven operation, low energy consumption, and precise emulation of synaptic plasticity, and can therefore be used universally for various neuromorphic electronic devices [9,13,16,17].

Recently-developed organic synaptic transistors exploit ion migration in the electrolyte and their electrochemical doping to the conjugated polymers [9,13,16]. Short and long-term synaptic behaviors of ion-gel gated organic synaptic transistor (IGOST) are caused primarily by migration of ions in the electrolyte dielectric to form electrostatic electric double layers (EDLs), and by electrochemical doping of ions into organic semiconductor (OSC), respectively [16]. Stable and heavy doping of ions into an OSC maintains increased conductance (i.e., synaptic weight) for a long time; the result is long-term retention and slow synaptic decay, which are important for neuromorphic computing and non-volatile memory. In contrast, short-term retention and fast synaptic decay are important for instant signal transmission of artificial sensory and motor nervous systems [18,19]. At this infant stage of organic neuromorphic devices, understanding the effect of OSC morphology on electrochemical-doping of ions and its synaptic plasticity is a critical importance to make effective devices for an intended use in neuromorphic computing and neuro-prosthetics. But until now, this has not been studied in organic synaptic transistors and there was no attempt to control the synaptic decay of single IGOST to make them applicable in diverse neuromorphic comupting and bioelectronic device systems: previous researches on organic synaptic transistors targeted only on single neuromorphic system that mimic either brains or biological afferent(sensory) nerves for either neuromorphic computing or neuro-prosthetics [9,18,20]. In conventional neuromorphic devices, to modulate the synaptic decay constant of the device from the short-term potentiation (STP) to long-term potentiation (LTP), the form of presynaptic spike (i.e., amplitude of spike, number of spikes etc.) was adjusted. Instead, tailoring of the synaptic properties of the devices in a fixed device using the same active material are necessary for broad applications.

In this study, we realized a synaptic-property-tunable IGOST using single intrinsic semiconducting polymer that emulate universal synaptic behaviors of both brain and peripheral nervous systems. We manipulated the morphology of OSC thin films to engineer electrochemical interaction between ions and OSC thin films in the IGOST. This process results in different synaptic decay behaviors so that the device mimics both cerebral computing and memory, and the responses of peripheral nerves depending on the morphologies of the polymer semiconductor films.

Depending on the crystallinity and grain size of OSC films, the IGOST showed a clear transition of synaptic responses between short-term potentiation (STP) and long-term potentiation (LTP) without adjusting the form of presynaptic spikes. The IGOST also demonstrated various synaptic properties such as paired-pulse facilitation (PPF), spike number dependent potentiation (SNDP), spike duration dependent potentiation (SDDP), spike frequency dependent potentiation (SFDP) and spike voltage dependent potentiation (SVDP). To prove the validity of our strategy, we performed simulations of pattern recognition of handwritten digits by highly crystalline IGOST with long synaptic decay and suggested that they have an accuracy of up to 94% and also developed an artificial auditory nerve that combines a triboelectric acoustic sensor and fast responsive IGOST with short synaptic decay.

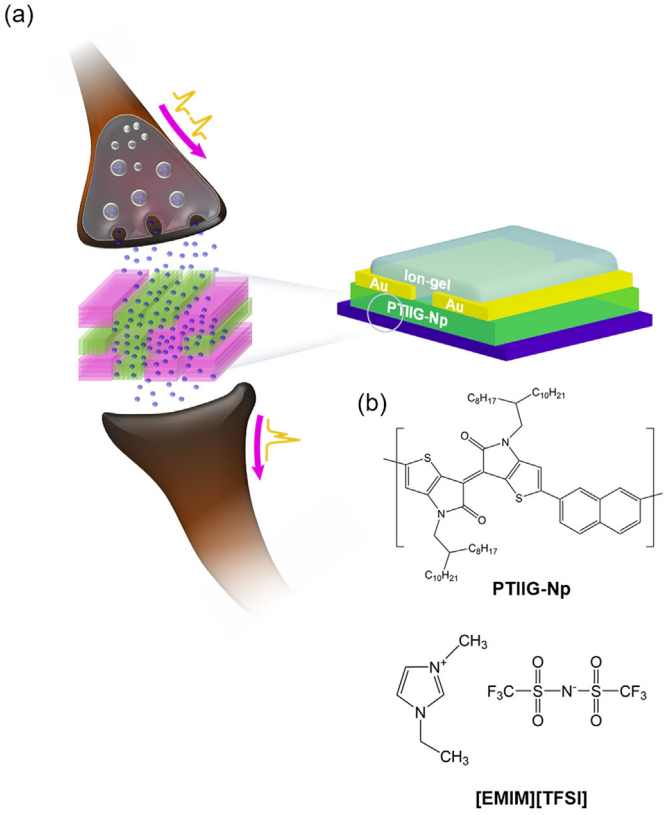

Fig. 1. (a) Schematics of biological synapse and structure of synaptic transistor. (b) Chemical structure of poly(thienoisoindigo-naphthalene) PTIIG-Np and 1-ethyl-3-methylimidazolium bis(trifluoromethylsulfonyl)imide ([EMIM][TFSI]). Alkyl side chain (R) is 2-octyldodecayl.

Table 1
Mobility, area of transfer curve and calculated charge carrier density N of PTIIG-Np IGOST.

Temperature (°C)	Mobility ($cm^2 \cdot V^{-1} \cdot s^{-1}$)	Area of Transfer Curve ($\times 10^{-5}$)	N ($\times 10^{26}$ m^{-3})
80	7	2.73	1.08
150	10	5.68	1.58
200	8	9.31	3.23
250	6	15.3	7.74
310	6	31.9	14.8

2. Experimental section

2.1. Device fabrication

Thin poly(thienoisoindigo-naphthalene) (molecular weight M_n = 36 kDa, PDI = 2.06) films were spincoated from a solution of 1,2-dichlorobenzene (~5 mg·ml^{-1}) on Si/SiO_2 (100 nm) substrate. Subsequently, the films were thermally annealed at 80, 150, 200, 250, or 310 °C for 10 min. Au source-drain electrodes (30 nm) were deposited by thermal evaporation. Ion-gel with poly(styrene–block-methyl methacrylate-block-styrene) (PS-PMMA-PS) and 1-ethyl-3-methylimidazolium bis(trifluoromethylsulfonyl)imide ([EMIM][TFSI]) in ethyl acetate (0.1:0.9:9, in weight) was drop cast on top of channel region and vacuum-annealed for 24 h at room temperature.

2.2. Measurement

Synchrotron-based GIXD was performed for all films at beamlines

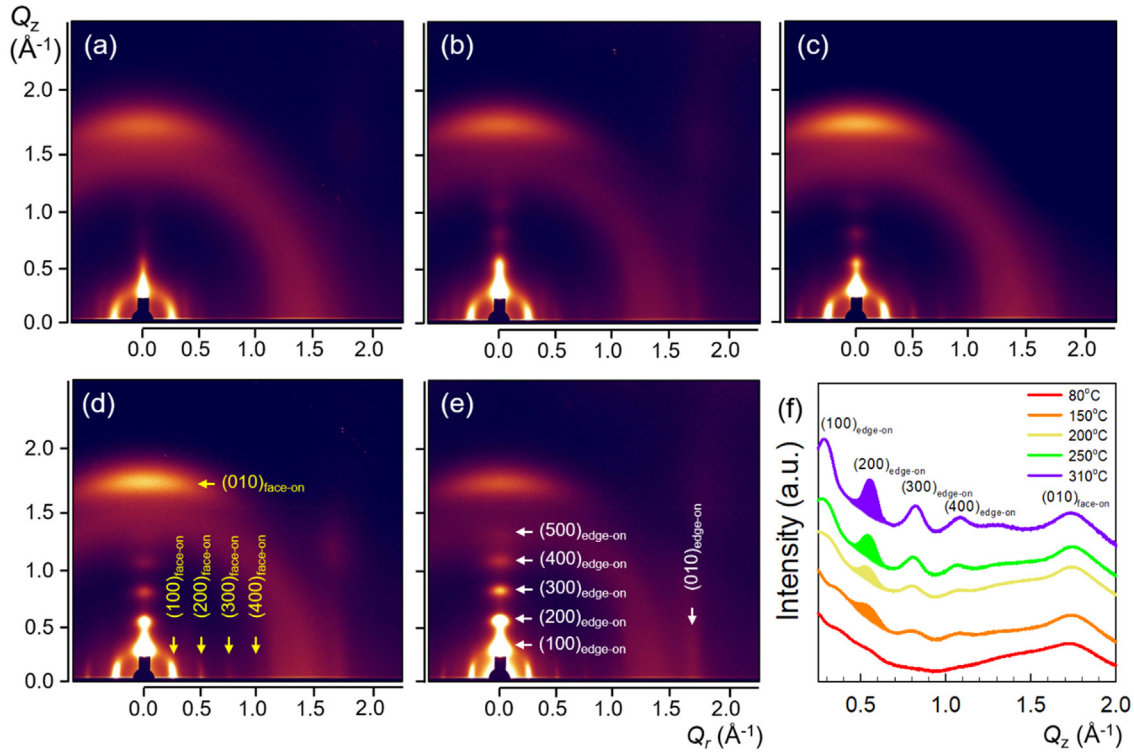

Fig. 2. (a–e) 2D GIXD patterns of PTIIG-Np films after thermal annealing at (a) 80 °C, (b) 150 °C, (c) 200 °C, (d) 250 °C, and (e) 310 °C. (f) 1D out-of-plane X-ray profiles extracted along the scattering vector Q_z axis from the 2D GIXD patterns of PTIIG-Np films.

Table 2
Variation in *d*-spacing and $\bar{G}$ of PTIIG-Np films after thermal annealing.

T_{ann} (°C)	$\triangle Q_{(100)}$ (Å^{-1})[a]	$d_{(100)}$ (Å)	$Q_{(010)}$ (Å^{-1})	$d_{(010)}$ (Å)[b]	FWHM ($Q_{(200)}$: Å^{-1})[c]	$\bar{G}$(Å)[d]
80	0.270	23.3	N/A	N/A	N/A	N/A
150	0.270	23.3	1.74	3.61	0.0938	120.7
200	0.260	24.2	1.74	3.61	0.0806	140.0
250	0.260	24.2	1.74	3.61	0.0641	176.1
310	0.260	24.2	1.73	3.63	0.0504	224.0

[a] Extracted along in-plane direction.
[b] Extracted along out-of-plane direction.
[c] Determined from $(200)_{edge\text{-}on}$ peaks.
[d] Grain size(D) = $K\lambda/(\beta\cos\theta)$; K = 0.9; λ = 1.0721 Å; θ = arcsin($q\lambda/4\pi$).

6D and 9A (Pohang Accelerator Laboratory, Republic of Korea). An incident angle of the X-ray beam (λ = 1.0721 Å) to a sample was fixed at 0.12°. Film morphologies were obtained using atomic force microscopy (AFM, Multimode 8, Bruker). UV-vis absorption spectra of films were measured using a UV-vis spectrophotometer (Lambda 465, PerkinElmer) at wavelengths from 190 nm to 1100 nm. Average number (M_n) and weight (M_w) molecular weights and PDI of the polymer was determined by high-temperature gel-permeation chromatography with Agilent 1200 HPLC and miniDAWN TREOS using a series of monodisperse polystyrene standards in 1,2,4-trichlorobenzene (HPLC grade) at 120 °C. FT-IR spectra were measured using a Fourier transform infrared spectrometer (TENSOR27, Bruker, Germany). The electric characteristics of the devices were measured using a Keysight B1500A semiconductor device analyzer.

2.3. Crossbar array simulation

The circuit simulation of artificial neural networks (ANNs) was simulated on the "CROSSSIM" platform developed at Sandia National Labatory, USA. The MNIST dataset of 60,000 handwritten digits was used for training and the MNIST dataset of 10,000 handwritten digits was used for testing the recognition accuracy. Backpropagation was used for training. To increase accuracy, a periodic carry with a 2-digit, base-5 system was used.

2.4. Sensor integration

A triboelectric sensor was layered with commercially available gold-coated textile and silver-coated textile (MedTex P180, Statex, Germany, Table S1) layers, and polytetrafluoroethylene (PTFE) to detect the sound wave generated from a speaker. PTFE is attached between the gold-coated textile layer and the silver-coated textile layer that is used as the electrode. Sound wave causes a periodic contraction and separation of the PTFE and the silver-coated textile layer; this oscillation results in back-and-forth motion of electrons due to the triboelectric effect. The triboelectric sensor was connected to an operational amplifier and bridge diode to amplify and rectify the output voltage from the sensor. Output voltage from the circuit was applied to the gate electrode of an IGOST.

3. Results and discussion

3.1. Film morphology control and I–V characterization

IGOST were fabricated with poly(thienoisoindigo-naphthalene) (PTIIG-Np) thin-film as an active layer, and 1-ethyl-3-methylimidazolium bis(trifluoromethylsulfonyl)imide ([EMIM][TFSI]) as an ion-gel dielectric (Fig. 1a). PTIIG-Np is a thienoisoindigo polymer with bicyclic lactam unit and thiophene derivative acceptor incorporated with a centrosymmetric acene naphthalene donor (Fig. 1b) that improves structural ordering, molecular packing and charge transport [21]. Also, alternative donor-acceptor copolymer units and the low-lying highest occupied molecular orbital (HOMO, -5.12 eV) may hinder electrochemical oxidation by ionic dopants compared to the homopolymer

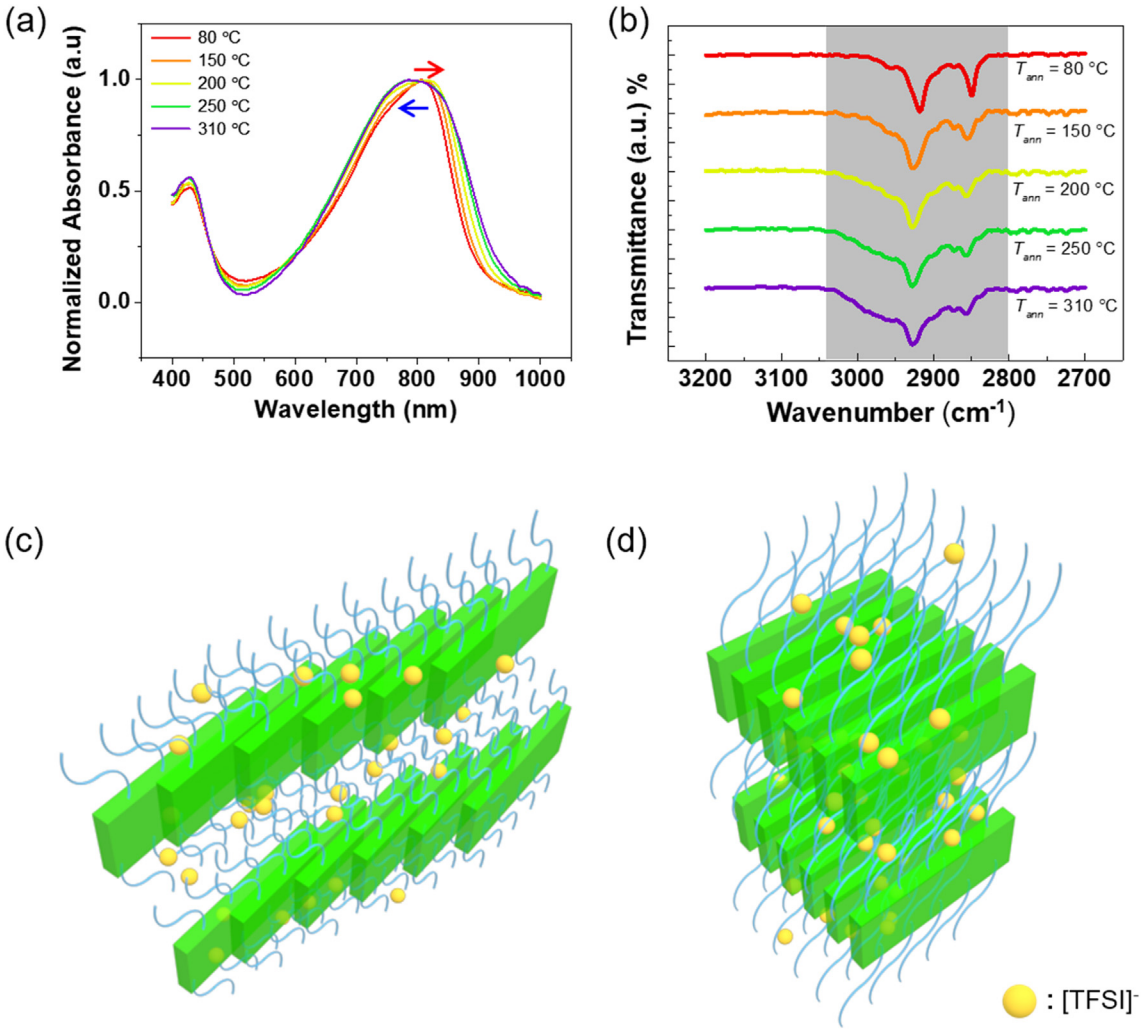

Fig. 3. (a) UV-vis absorption and (b) FT-IR spectra of PTIIG-Np films annealed at 80, 150, 200, 250, or 310 °C. Blue-shift in C-H stretch region (2956 – 2855 cm^{-1}) is attributed to increased interaction between alky side-chains. Schematic illustrations of (c) J- and (d) H-aggregates in PTIIG-Np films.

poly(3-hexylthiophene) (P3HT) with HOMO energy level ~ -4.7 eV [21,22]. The low doping efficiency would provide more electrochemical window to enable precise control of ion doping of IGOST for demonstration of wide range of synaptic decays in various neuromorphic electronics. Therefore, change of thermal annealing temperature on the polymer film can cause more sensitive variation of synaptic behaviors.

At low annealing temperature T_{ann}, OSC thin film has low crystallinity and large grain boundaries (GBs). With sufficient amplitude of presynaptic voltage pulses, ions migrate to the surface of OSC film and penetrated mainly through GBs. The penetrated ions can also easily diffuse back into the gel electrolyte medium through GBs; this process causes fast synaptic decay. As T_{ann} increases, together with enhancement of crystallinity and grain size of OSC, the number of GBs diminished, leading to boosting the proportion of grains in the films. Therefore, with the same presynaptic voltage pulses, a large number of ions are driven into the crystalline domains, at the same time, making difficult to proceed the spontaneous back diffusion of embedded ions. This process extends the retention of synaptic current. To explore the morphological change effect on synaptic decay of IGOST, we annealed OSC films at T_{ann} = 80, 150, 200, 250 and 310 °C (because there was considerable weight loss with higher temperature (Fig. S1) and the decomposition of polymer film would cause degradation of electrical characterisitcs (Fig. S2) the OSC film was annealed up to 310 °C).

The drain current-gate voltage (I_D-V_G) transfer curve was measured in ambient condition with a sweep rate of 75 mV·s^{-1} (Fig. S2). The carrier mobility of IGOST was calculated by considering the total induced hole density P_i [23–25].

$$P_i = \left[\int I_{Disp} dV_G\right] \Big/ \left[(dV_G/dt)\cdot e\cdot A\right] \quad (1)$$

where $e = 1.6 \times 10^{-19}$ C is electron elementary charge and A [cm^2] is channel area, and gate-displacement current (I_{Disp} [A]) was calculated by integrating the gate current-gate voltage (I_G-V_G) curve. Carrier mobility (μ) was then calculated as $\mu = (L/W)\cdot[I_D/(V_D\cdot eP_i)]$, where I_D [A] is drain current, V_D [V] is drain voltage, L [cm] is channel length and W [cm] is channel width [25]. Using calculated μ and I_{Disp}, we obtained charge carrier density (N) from the I_D-V_G curve by integrating I_D over dV_G (Table 1 and Supplementary Note). As T_{ann} increased, N also increased (Table 1). N is a result of doped ions that did not instantly diffuse back into the ion-gel medium during voltage sweep. As the number of trapped ions increases, the number of charge carriers also increases, so an increase in N can be considered to be a result of increased numbers of trapped ions in the active layer. The device annealed at 310 °C had the largest number of trapped ions (Table 1). This trend can be attributed to an enhanced crystallinity with an increase in T_{ann}.

To quantify how T_{ann} affected the OSC films, we used grazing incidence X-ray diffraction (GIXD) to measure their crystal structures (Fig. 2). At T_{ann} = 80 °C, the films had almost disordered structure with

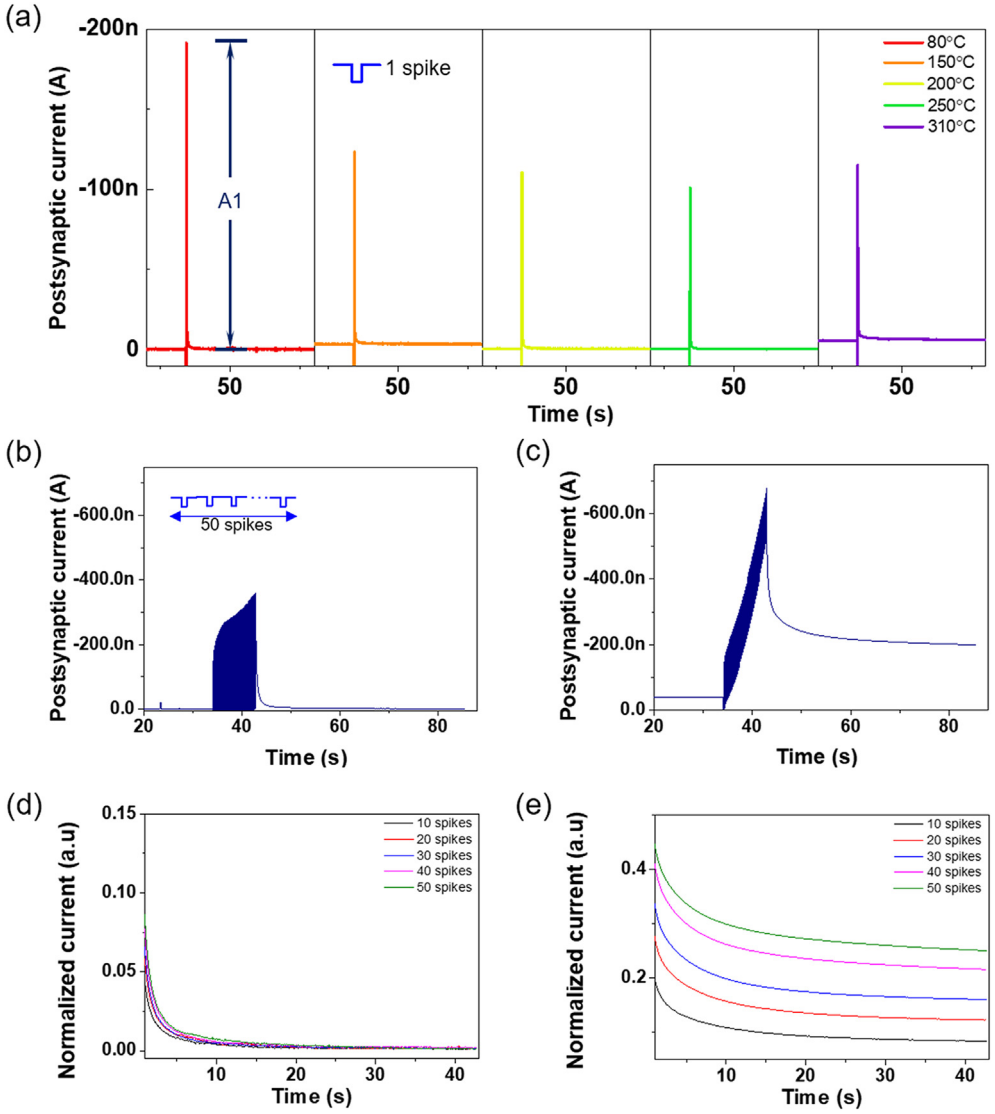

Fig. 4. (a) Synaptic responses of IGOST with T_{ann} = 80, 150, 200, 250, or 310 ℃ by applying single presynaptic spike (V_G = -2.5 V, 80 ms) with V_D of -100 mV as postsynaptic voltage to read current. EPSC of IGOST with (b) T_{ann} = 80 and (c) 310 ℃ after 50 presynaptic voltage spikes (V_G = -2.5 V, 80 ms). Normalized synaptic decay curves of IGOST with films prepared at (d) T_{ann} = 80 ℃ and (e) T_{ann} = 310 ℃ after multiple presynaptic voltage spikes (V_G = -2.5 V, 80 ms). Drain voltage V_D = -100 mV was applied to read postsynaptic current.

Table 3
Changes in of τ_1, τ_2 and τ_3 of IGOST after 50 presynaptic spikes according to annealing temperature T_{ann}.

T_{ann} (℃)	τ_1 (s)	τ_2 (s)	τ_3 (s)
80	0.07432	0.5999	8.555
150	0.08351	0.5622	10.98
200	0.1412	2.242	99.84
250	0.2086	3.114	144.4
310	0.2265	3.593	230.1

very low crystallinity (Fig. 2a and Fig. S3a). The crystallinity increased gradually with an increase in T_{ann} and at T_{ann} = 310 ℃, crystallinity and average grain size ($\bar{G}$) showed the highest value (Fig. 2a–e and Table 2). One-dimensional (1D) line profile demonstrated an increase in crystallinity (Fig. 2f). As T_{ann} increased, the (010) peaks, which correspond to π-π overlapped distance between PTIIG-Np polymer chains, were sharpened at both in-plane and out-of-plane directions (Fig. 2f and Fig. S3f).

In addition, full-width at half maximum (FWHM) of $(200)_{edge\text{-}on}$ reflection became narrow; this change indicates that $\bar{G}$ of PTIIG-Np films increased (Fig. 2a–f and Table 2). Note that $(200)_{edge\text{-}on}$ reflection were used, instead of $(100)_{edge\text{-}on}$ ones including intense specular background (Fig. 2f). FWHM could not be defined in the film with T_{ann} = 80 ℃, owing to too low crystallinity. The FWHM value was 0.0938 $Å^{-1}$ at T_{ann} = 150℃, and 0.0504 $Å^{-1}$ at T_{ann} = 310 ℃; this trend indicates an increase in $\bar{G}$, as calculated by Scherrer equation [26]. The criterion for subtracting the background may cause systematic errors, so it is better considering the trend in change rather than the calculated values. Calculated $\bar{G}$ values increased as T_{ann} increased from 150 to 310 ℃ (Table 2). Tapping mode atomic force microscopy (AFM) images also agreed with this trend of $\bar{G}$ (Figs. S3a–e). As T_{ann} increased, surface roughness (RMS) value of films also increased (0.440 nm at T_{ann} = 80 ℃, and 0.780 nm at T_{ann} = 310 ℃). This trend is likely due to increased crystallization and ordering of the copolymer during the annealing process [27,28]. Therefore, T_{ann} changes the morphology of the OSC films, and this change leads to variation in their ion diffusion and trapping properties.

In UV-vis absorption spectra of different T_{ann} OSC films the absorption maximum peak was redshifted from 804 nm (at T_{ann} = 80 ℃)

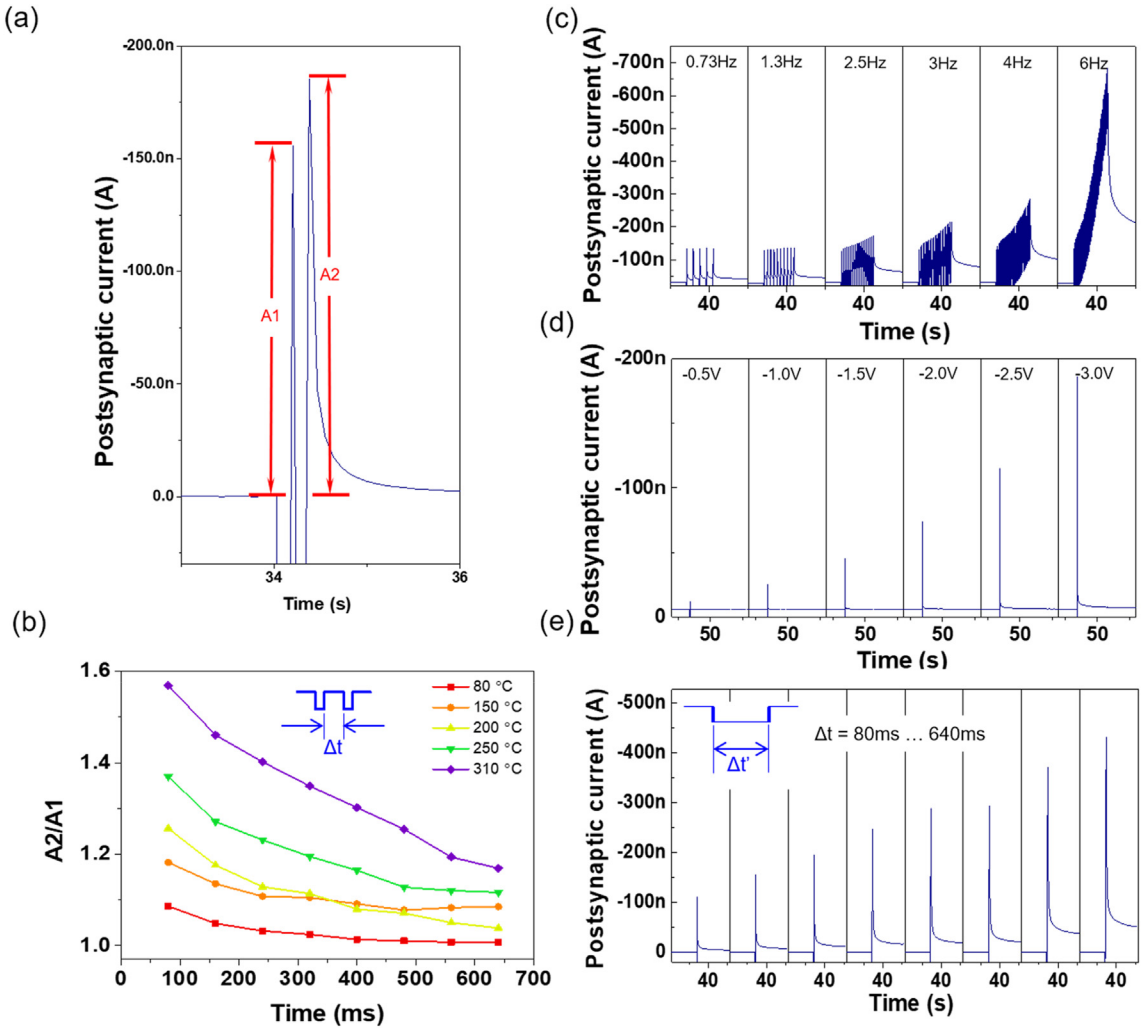

Fig. 5. Various synaptic property of IGOST. (a) EPSC of IGOST with films prepared at T_{ann} = 80 ℃ after two presynaptic spikes with -2.5 V and 80 ms. (b) PPF index as time interval between spikes increase. (c) SFDP of IGOST with films prepared at T_{ann} = 310 ℃. Presynaptic spike frequency to measure SFDP were 0.73, 1.3, 2.5. 3.0, 4.0, and 6.0 Hz (V_G = -2.5 V, 80 ms, V_D = -0.1 V). (d) SVDP of IGOST with films prepared at T_{ann} = 310 ℃. SVDP was measured on presynaptic spike of -3.0 ≤ V_G ≤ -0.5 V in increments of 0.5 V with fixed spiking time (80 ms, V_D = -0.1 V). (e) SDDP of IGOST with films prepared at T_{ann} = 310 ℃. SDDP was measured on fixed V_G = -2.5 V while varying the spike duration (80 ≤ Δt' ≤ 640 ms in increments of 80 ms).

to 813 nm at (T_{ann} = 200 ℃), originated from an increased π-conjugated length in the interchain (Fig. 3a) [29]. When branched alkyl side-chain substituted semicoducting polymer, such as PTIIG-Np, forms an ordered conformation during solution casting, a steric hindrance by these alkyl side chains impedes overlapping of π-conjugated backbone chains [27]. Therefore, at relatively low T_{ann}, PTIIG-Np chains formed a partially π-conjugated chain conformation with a J-aggregate (Fig. 3a, c). However, when T_{ann} (e.g., 250 and 310 ℃) is enoguh high to form an intermolecular π-overlapped structure with an H-aggregate, it was found that the absorption maximum peak blue shifted from 813 nm to 786 nm (at T_{ann} = 250 ℃) and 785 nm at (T_{ann} = 310 ℃) (Fig. 3a) [30]. High T_{ann} provides sufficient energy for molecular redistribution, so transition from J-to H-aggregate can occur (Fig. 3a, d) [30].

From the FT-IR spectra, (Fig. 3b), all the films showed peaks in the C−H stretching region (2956 − 2855 cm^{-1}) which is attributed to alkyl side-chains [31]. As annealing temperature increased, the peaks in C−H stretch region were blue-shifted because of increased interaction between alkyl side-chains. High T_{ann} provides thermal energy enough to overcome steric hindrance between alkyl side-chains and may change alignment in polymers. Therefore, as T_{ann} increases, the crystallinity of the films increases, and morphological transition restricts spontaneous diffusion of ions from crystal domains and prolongs ion trapping.

3.2. Synaptic characteristics

Presynaptic voltage spikes (-2.5 V, 80 ms) were applied to the gate electrode, and drain voltage V_D (-0.1 V) was applied to read the postsynaptic current. A presynaptic spike of -2.5 V is considered to be sufficient to drive ions to penetrate into the crystalline region of the donor-acceptor copolymer film with low electrochemical doping efficiency [32]. Presynaptic spike causes ion migration in ion-gel, then triggers excitatory postsynaptic current (EPSC). The peak was -191.5 nA in devices including films prepared at T_{ann} = 80 ℃, and the magnitude decreased as T_{ann} increased (-123.4 nA at T_{ann} = 150 ℃, -110.6 nA at T_{ann} = 200 ℃, -101.0 nA at T_{ann} = 250 ℃, -109.4 nA at T_{ann} = 310 ℃) (Fig. 4a).

This decrease in the EPSC peak can be attributed to the morphological difference of OSC thin films. When a single presynaptic pulse is applied, many ions are more likely to move through GBs than to penetrate into the crystalline region. Therefore, EPSC in films with low crystallinity would be large because numerous ions can enter the large GB regions of the films. In contrast, highly-crystalline films have relatively small GBs, so EPSC should be small. However, when multiple consecutive pulses (i.e., up to 50 pulses) are applied, most of the ions will enter the GBs of low-crystallinity films, but will easily diffuse back

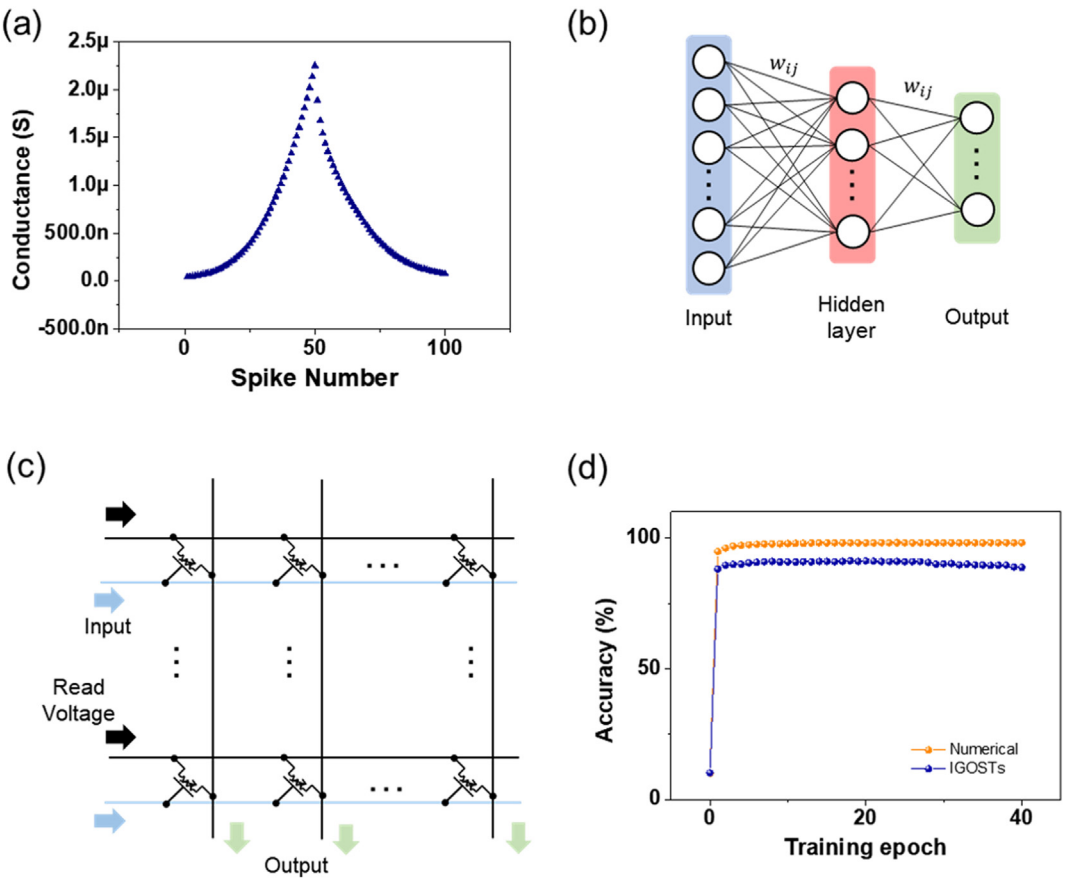

Fig. 6. Multi-conductance state and MNIST recognition simulation of IGOST. (a) Conductance states with 50 write (-2.5 V, 80 ms) and 50 erase (1.0 V, 80 ms) pulses. Drain voltage V_D = -100 mV was applied to read postsynaptic current for ~4.7 s. CROSSSIM was used to simulate recognition accuracy of handwritten digits. (b) Schematics of MNIST recognition simulation. Artificial neural network with one hidden layer (300 neurons) is simulated. (c) Schematics of IGOST crossbar array used in simulation. (d) Recognition accuracy in 28 × 28 MNIST hand written digits of ideal numerical devices compared to the IGOST. 40 epochs were performed.

when the voltage pulse is removed, so EPSC will not increase significantly (Fig. 4b, d). On the other hand, in high-crystallinity films, numerous ions will enter the large grain domains, and cannot escape easily after the pulse is removed, so EPSC increases significantly (Fig. 4c, e).

We fabricated IGOST including films that had been annealed at different T_{ann}, then subjected them to a range of electrical stimuli. We denote these IGOST as $IGOST_n$, where n = T_{ann}. These IGOST had distinct responses.

We first tested how the number n_{pre} of presynaptic spikes affected the retention in the change of postsynaptic current. As n_{pre} was increased from 10 to 50, the decay curves of IGOST diverged. $IGOST_{80}$ showed no significant difference in current decay curves (Fig. 4d), but $IGOST_{310}$ showed clear transition from short retention to long retention of postsynaptic current (Fig. 4e). Therefore, this use of a range of T_{ann} controls the synaptic responses of IGOST from STP to LTP and enables fabrication of IGOST that are applicable for not only brain-inspired memory and computing due to emulation of long retention but also artificial afferent/efferent nerves due to emulation of short retention (Fig. S5).

The relaxation curves of synaptic weight for IGOST (Fig. 4e and Fig. S6d) are similar to the forgetting curve of a brain [14], which can be expressed by an exponential decay curve [33]. In this study, we used a tri-exponential function to express the decay of synaptic weight W over time:

$$W = A \cdot e^{-x/\tau_1} + B \cdot e^{-x/\tau_2} + C \cdot e^{-x/\tau_3}, \quad (2)$$

where x is elapsed time during decay; A, B and C are constants; τ_1 [s], τ_2 [s], and τ_3 [s], are relaxation-time constants that correspond respectively to the relaxation of ions from EDLs, from amorphous/GB regions, and from crystalline regions of OSC thin films. τ_3 is related to long–term memory retention; the value of τ_3 after application of 50 presynaptic spikes increased from 8.6 s in $IGOST_{80}$ to 230.1 s in $IGOST_{310}$ (Table 3 and Fig. S7). This tendency of increase in decay time fits well with the morphological change of the device; this result means synaptic decay characterisitcs of the IGOST can be controlled from STP-dominant to LTP-dominant.

We also observed the PPF property of IGOST (Fig. 5a and b). Two consecutive spikes (-2.5 V, 80 ms) with different time intervals (80 ≤ Δt ≤ 640 ms in increments of 80 ms) were applied to the gate electrode. The height A_1 of the first EPSC peak and the height A_2 of the second EPSC peak were used to calculate the PPF index A_2/A_1 (Fig. 5a). As Δt increased, A_2/A_1 decreased due to the spontaneous back diffusion of anions. $IGOST_{80}$ had the fastest current decay, so they showed the smallest A_2/A_1 = 1.09 (at Δt = 80 ms) (Fig. 5b). $IGOST_{310}$ showed the highest A_2/A_1 = 1.57 (at Δt = 80 ms) because of electrochemical doping of diffused ions in the highly crystalline films.

Synaptic responses were also affected by spike frequency, spike amplitude and spike duration. As stimuli were strengthened (i.e., by increase in frequency, in amplitude, or in duration), EPSC increased (Fig. 5c–e and Figs. S8–S10). As the frequency of the presynaptic device increases, both EPSC and EPSC gain (A_{10}/A_1) increased (Fig. S8e). In a biological synapse, presynaptic spike frequency is related to the firing of the postsynaptic spikes. This change in the responses of the IGOST is similar to the dynamic high-pass filtering function of a biological synapse [2,34].

For neuromorphic electronics implementing artificial neural networks (ANNs), analog input vectors are presented in the voltage

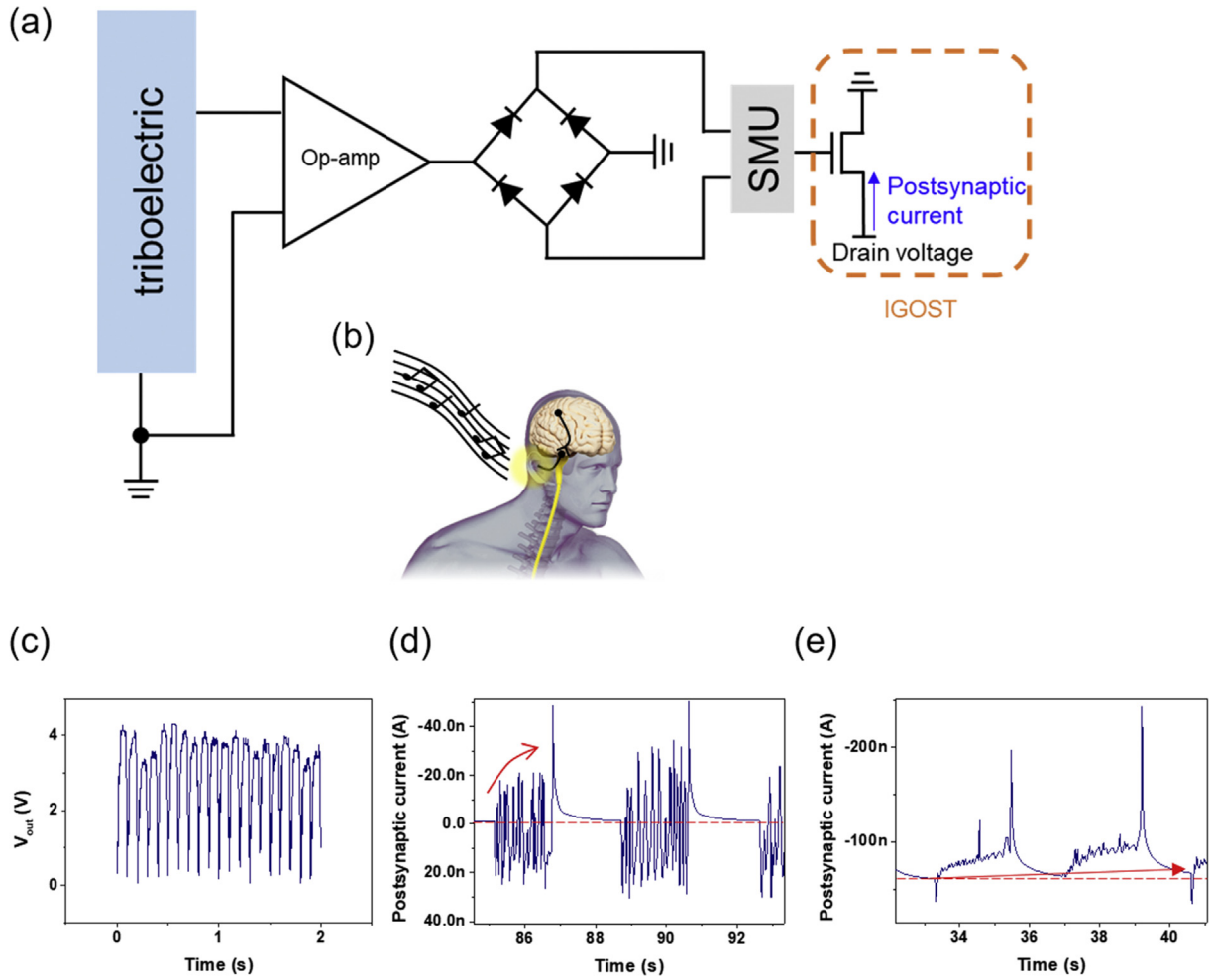

Fig. 7. Artificial auditory systems using IGOST and triboelectric devices. (a) A circuit diagram of an auditory nerve system. A triboelectric device was used to detect the sound wave and IGOST was connected. To amplify the voltage from the triboelectric device, operative amplifier was used. A rectifier changes bidirectional output signals to unidirectional output. (b) Schematics of human auditory nerve systems. (c) Supplying voltage to IGOST with 5 Hz square sound wave applied to triboelectric device. Postsynaptic current measured from IGOST with (d) films prepared at 80 °C and (e) films prepared at 310 °C.

amplitude or the pulse length [7,35]. Thus, these responses to presynaptic spike voltage amplitude and pulse length indicate that IGOST can be used in neuromorphic electronics.

3.3. Synaptic decay dependent neuromorphic electronics

For synaptic transistors to be used as neuromorphic devices in ANNs, systemically programmable conductance states are required [36]. With a series of 50 negative spikes (-2.5 V) and 50 positive spikes (1.0 V), $IGOST_{310}$, which had the most stable long-term memory, showed symmetric potentiation/depression states (Fig. 6a). With this result, we simulated ANNs to recognize MNIST handwritten digit data by performing backpropagation [9,37,38]. For the simulation, 8×8 [39] and 28×28 MNIST data [40] were unwrapped to 1×64 and 1×784 row vectors to perform vector matrix multiplication. One hidden layer with 300 hidden neurons was used and 10 output neurons that correspond to 10 classes of digits ($0-9$) were used (Fig. 6b). Simulation was performed for a crossbar array (Fig. 6c); 60,000 images were used for supervised backpropagation training, and 10,000 were used to test the recognition accuracy [40]. We simulated total 40 epochs for the ANNs in ideal numerical and IGOST. Trained IGOST showed accuracy of 94.49% for 8×8 MNIST data, and 91.29% for 28×28 MNIST data (Fig. 6d and Fig. S11c). These high accuracies indicate that morphology-engineered IGOST with stable long-term memory property can be used for ANNs computing.

IGOST with fast response and rapid synaptic decay are applicable to emulate biological sensory nervous system such as cochlear nuclei of the auditory system, in which synapse facilitation takes tens of milliseconds to recover [41–43]. We demonstrated artificial auditory synapses with acoustic sensors (triboelectric sensors) and IGOST (Fig. 7a and b). Rectified output voltage pulses from acoustic sensors were applied to the gate electrodes of IGOST (Fig. 7c). $IGOST_{80}$ (τ_3 = 8.6 s) and $IGOST_{310}$ (τ_3 = 230.1 s) were compared. A square sound wave of 5 Hz was generated from a speaker. For $IGOST_{80}$, the 5 Hz sound wave induced EPSC potentiation that decayed rapidly (< 1 s) after the sound was turned off (Fig. 7d). In contrast, for $IGOST_{310}$, the sound wave induced LTP of EPSC and slow synaptic decay, which resulted resting current increase after repeated sound detection (Fig. 7e); this result impedes sensitive response of artificial sensory nervous system. This engineering in IGOST allows development of customized artificial synapses for versatile neuromorphic electronics.

4. Conclusion

We achieved different synaptic decay times in single IGOST without changing organic semiconducting polymer and device geometry but by controlling the morphological properties of the polymer film. As polymer crystallinity changed, the synaptic decay properties of the devices changed from STP-dominant to LTP-dominant. Furthermore, engineering the synaptic decay time constant by changing the

crystallinity revealed the relationship between the synaptic property and morphological property in IGOST. Although devices which used films that had been prepared at T_{ann} = 310 ℃ showed feasible MNIST recognition accuracy by 94.49% for 8 × 8 MNIST data and 91.29% for 28 × 28 MNIST data with LTP-dominant synaptic decay property, they were not suitable for an artificial sensory nervous system. In contrast, devices which used films that had been prepared at T_{ann} = 80 ℃ showed appropriate characteristic for artificial sensory nervous system, with STP-dominant synaptic decay property. Circuit simulation of IGOST and their integration with sensors demonstrated that the engineering the microstructure of the polymer film is imperative for the specific emulation of synaptic behavior that is suitable for specific neuromorphic applications (i.e. mimicking either the central or peripheral nerve system). This is the first report to show how to engineer the decay-time constant of the device by changing the morphology of the thin film in a single device, rather than changing the form of presynaptic spikes. Various synaptic functions such as SNDP, PPF, SFDP, SVDP, and SDDP were reproduced in a single device. This work presents a new strategy to engineer a required property in organic synaptic transistors for various potential applications such as neuromorphic computing, neural prosthetics, bio-interface devices, and soft robotics.

Acknowledgements

D.-G. S. and Y. L. equally contributed to this work. This work was supported by the National Research Foundation of Korea (NRF) grant funded by the Korea government (Ministry of Science, ICT & Future Planning) (NRF-2016R1A3B1908431, NRF2017R1A2B4009313). This work was also supported by the Center for Advanced Soft-Electronics funded by the Ministry of Science and ICT as Global Frontier Project (2013M3A6A5073175), and Creative-Pioneering Researchers Program through Seoul National University (SNU).

Appendix A. Supplementary data

Supplementary data to this article can be found online at https://doi.org/10.1016/j.nanoen.2019.104035.

References

[1] V.M. Ho, J.-A. Lee, K.C. Martin, Science 334 (2011) 623–628.
[2] L.F. Abbott, W.G. Regehr, Nature 431 (2004) 796–803.
[3] J.F. Otto, Y. Yang, W.N. Frankel, H.S. White, K.S. Wilcox, J. Neurosci. 26 (2006) 2053–2059.
[4] M.A. Ungless, X. Gasull, E.T. Walters, J. Neurophysiol. 87 (2002) 2408–2420.
[5] A.L. Hodgkin, A.F. Huxley, J. Physiol. 117 (1952) 500–544.
[6] E.M. Izhikevich, IEEE Trans. Neural Netw. 14 (2003) 1569–1572.
[7] M. Hu, C.E. Graves, C. Li, Y. Li, N. Ge, E. Montgomery, N. Davila, H. Jiang, R.S. Williams, J.J. Yang, Q. Xia, J.P. Strachan, Adv. Mater. 30 (2018) 1705914.
[8] P. Yao, H. Wu, B. Gao, S.B. Eryilmaz, X. Huang, W. Zhang, Q. Zhang, N. Deng, L. Shi, H.P. Wong, H. Qian, Nat. Commun. 8 (2017) 15199.
[9] Y. Van De Burgt, E. Lubberman, E.J. Fuller, S.T. Keene, G.C. Faria, S. Agarwal, M.J. Marinella, A. Alec Talin, A. Salleo, Nat. Mater. 16 (2017) 414–418.
[10] W. Wang, G. Pedretti, V. Milo, R. Carboni, A. Calderoni, N. Ramaswamy, A.S. Spinelli, D. Ielmini, Sci. Adv. 4 (2018) 4752 eaat.
[11] M. Prezioso, M.R. Mahmoodi, F.M. Bayat, H. Nili, H. Kim, A. Vincent, D.B. Strukov, Nat. Commun. 9 (2018) 5311.
[12] W. Xu, H. Cho, Y.H. Kim, Y.T. Kim, C. Wolf, C.G. Park, T.W. Lee, Adv. Mater. 28 (2016) 5916–5922.
[13] P. Gkoupidenis, N. Schaefer, B. Garlan, G.G. Malliaras, Adv. Mater. 27 (2015) 7176–7180.
[14] B.-Y. Kim, H.-G. Hwang, J.-U. Woo, W.-H. Lee, T.-H. Lee, C.-Y. Kang, S. Nahm, NPG Asia Mater. 9 (2017) e381.
[15] G. Wu, P. Feng, X. Wan, L. Zhu, Y. Shi, Q. Wan, Sci. Rep. 6 (2016) 23578.
[16] W. Xu, S.-Y. Min, H. Hwang, T.-W. Lee, Sci. Adv. 2 (2016) e1501326.
[17] S.-I. Kim, Y. Lee, M.-H. Park, G.-T. Go, Y.-H. Kim, W. Xu, H.-D. Lee, H. Kim, D.-G. Seo, W. Lee, T.-W. Lee, Adv. Electron. Mater. 0 (2019) 1900008.
[18] Y. Kim, A. Chortos, W. Xu, Y. Liu, J.Y. Oh, D. Son, J. Kang, A.M. Foudeh, C. Zhu, Y. Lee, S. Niu, J. Liu, R. Pfattner, Z. Bao, T.-W. Lee, Science 360 (2018) 998–1003.
[19] Y. Lee, J.Y. Oh, W. Xu, O. Kim, T.R. Kim, J. Kang, Y. Kim, D. Son, J.B.-H. Tok, M.J. Park, Z. Bao, T.-W. Lee, Sci. Adv. 4 (2018) eaat7387.
[20] T.-Y. Wang, Z.-Y. He, H. Liu, L. Chen, H. Zhu, Q.-Q. Sun, S.-J. Ding, P. Zhou, D.W. Zhang, ACS Appl. Mater. Interfaces 10 (2018) 37345–37352.
[21] G. Kim, S.J. Kang, G.K. Dutta, Y.K. Han, T.J. Shin, Y.Y. Noh, C. Yang, J. Am. Chem. Soc. 136 (2014) 9477–9483.
[22] D. Di Nuzzo, C. Fontanesi, R. Jones, S. Allard, I. Dumsch, U. Scherf, E. Von Hauff, S. Schumacher, E. Da Como, Nat. Commun. 6 (2015) 6460.
[23] J. Lee, L.G. Kaake, J.H. Cho, X.-Y. Zhu, T.P. Lodge, C.D. Frisbie, J. Phys. Chem. C 113 (2009) 8972–8981.
[24] Y. Xia, J. Cho, B. Paulsen, C.D. Frisbie, M.J. Renn, Appl. Phys. Lett. 94 (2009) 10–13.
[25] Y. Xia, J.H. Cho, J. Lee, P.P. Ruden, C.D. Frisbie, Adv. Mater. 21 (2009) 2174–2179. Adv. Mater. 21 (2009) 2174–2179.
[26] A.L. Patterson, Phys. Rev. 56 (1939) 978–982.
[27] T. Lei, Y. Cao, X. Zhou, Y. Peng, J. Bian, J. Pei, Chem. Mater. 24 (2012) 1762–1770.
[28] M.S. Chen, O.P. Lee, J.R. Niskala, A.T. Yiu, C.J. Tassone, K. Schmidt, P.M. Beaujuge, S.S. Onishi, M.F. Toney, A. Zettl, J.M.J. Fréchet, J. Am. Chem. Soc. 135 (2013) 19229–19236.
[29] T. Lei, Y. Cao, Y. Fan, C. Liu, S. Yuan, J. Pei, J. Am. Chem. Soc. 133 (2011) 6099–6101.
[30] A. Sarbu, L. Biniek, J.M. Guenet, P.J. Mésini, M. Brinkmann, J. Mater. Chem. C. 3 (2015) 1235–1242.
[31] D.M. Delongchamp, R.J. Kline, D.A. Fischer, L.J. Richter, M.F. Toney, Adv. Mater. 23 (2011) 319–337.
[32] J.O. Guardado, A. Salleo, Adv. Funct. Mater. 27 (2017) 1701791.
[33] P.A. Wozniak, E.J. Gorzelanczyk, J.A. Murakowski, Acta Neurobiol. Exp. 55 (1995) 301–305.
[34] P. Gkoupidenis, N. Schaefer, X. Strakosas, J.A. Fairfield, G.G. Malliaras, Appl. Phys. Lett. 107 (2015) 263302.
[35] D. Kadetotad, Z. Xu, A. Mohanty, P. Chen, B. Lin, J. Ye, S. Vrudhula, S. Yu, Y. Cao, J. Seo, IEEE J. Emerg. Sel. Top. Circuits Syst. 5 (2015) 194–204.
[36] Y. van de Burgt, A. Melianas, S.T. Keene, G. Malliaras, A. Salleo, Nat. Electron. 1 (2018) 386–397.
[37] E.J. Fuller, F. El Gabaly, F. Léonard, S. Agarwal, S.J. Plimpton, R.B. Jacobs-Gedrim, C.D. James, M.J. Marinella, A.A. Talin, Adv. Mater. 29 (2017) 1604310.
[38] S. Agarwal, S.J. Plimpton, D.R. Hughart, A.H. Hsia, I. Richter, J.A. Cox, C.D. James, M.J. Marinella, Int. Jt. Conf. Neural Networks 2016 (2016) 929–938.
[39] D. Dua, C. Graff, UCI Machine Learning Repository, (2017) http://archive.ics.uci.edu/ml/ , Accessed date: 1 January 2019.
[40] Y. Lecun, L. Bottou, Y. Bengio, P. Haffner, IEEE 86 (1998) 2278–2324.
[41] T. Kuenzel, J.G.G. Borst, M. van der Heijden, J. Neurosci. 31 (2011) 4260–4273.
[42] S. Bleeck, M. Sayles, N.J. Ingham, I.M. Winter, Hear. Res. 212 (2006) 176–184.
[43] K.M. MacLeod, T.K. Horiuchi, C.E. Carr, J. Neurophysiol. 97 (2007) 2863–2874.

Dae-Gyo Seo received his B.S. (2018) in Department of Materials Science and Engineering from Korea University, Korea. He is studying for his Ph.D. course in the Department of Materials Science and Engineering of Seoul National University. His research interest includes the organic transistors, neuromorphic electronics, and artificial nerve systems.

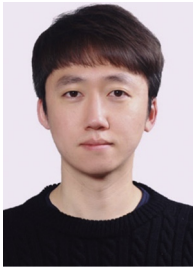

Yeongjun Lee is a postdoctoral researcher in Materials Science and Engineering at Seoul National University, Korea. He received his M.S. (2014) and Ph.D. (2018) in Materials Science and Engineering from Pohang University of Science and Technology (POSTECH), Korea. His research interests include printed electronics, nanowire electronics, stretchable polymer electronics, and organic neuromorphic electronics.

Gyeong-Tak Go is studying for his Ph.D Course in the Department of Materials Science and Engineering of Seoul National University. His research interests include the organic neuromorphic electronics based on artificial synapse devices.

Mingyuan Pei is currently studying for Ph.D. degree under the supervision of Prof. Hoichang Yang from Department of Chemical Engineering at Inha University, Korea. He received his B.S. and M.S. degree from the Department of Materials Engineering at Tianjin Polytechnic University in 2011 and 2014, respectively. His research focuses on the structure and performance of organic thin film transistors.

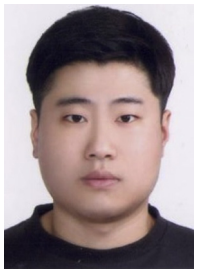

Sungwoo Jung is in the combined master's and doctorate course for Energy Engineering in Ulsan National Institute of Science and Technology (UNIST). He received B.S. in 2017 Energy Engineering from UNIST. He joined Professor Changduk Yang's group in 2017 and his main research focus is on synthesizing organic materials which will be applied for optoelectronic devices and triboelectric nanogenerator.

Yo Han Jeong is a Master with Prof. Sang-Woo Kim at SKKU Advanced Institute of Nanotechnology (SAINT), Sungkyunkwan University (SKKU). His research interests are DFT simulation related with new materials for nanogenerators and 2D materials.

Wanhee Lee is an undergraduate studying in the Department of Physics and Astronomy at Seoul National University. His research interests include device simulation for neuromorphic computing and first principle description of atoms and molecules on two-dimensional materials.

Hea-Lim Park has joined Prof. Lee's group since 2018 as a postdoctoral researcher. She received her Ph.D. at the School of Electrical Engineering, Seoul National University, Republic of Korea in 2018. She received her B.S. degree in electrical and electronic engineering from Yonsei University in 2012. Her current research interests include organic transistors, sensors, and bio-inspired neuromorphic devices.

Sang-Woo Kim is an Associate Professor in School of Advanced Materials Science and Engineering at Sungkyunkwan University (SKKU). He received his Ph.D. from Kyoto University in Department of Electronic Science and Engineering in 2004. After working as a postdoctoral researcher at Kyoto University and University of Cambridge, he spent 4 years as an assistant professor at Kumoh National Institute of Technology. He joined the School of Advanced Materials Science and Engineering, SKKU Advanced Institute of Nanotechnology (SAINT) in 2009. His recent research interest is focused on piezoelectric/triboelectric nanogenerators, photovoltaics, and two-dimensional nanomaterials including graphene and hexagonal boron nitride nanosheets.

Hoichang Yang is currently a professor at the Department of Chemical Engineering, Inha University since 2009. He received his Ph.D. from Chemical Engineering, Pohang University of Science and Technology (POSTECH) in 2002. He had been a senior researcher at the Rensselaer Nanotechnology Center in Rensselaer Polytechnic Institute (2003–2008). His research interest are in the field of surface/interface engineering, self-assembly related to energy and organic electronic applications, specifically, organic thin film transistors.

Changduk Yang obtained his Ph.D. degree from the Max Plank Institute for Polymer Research (Germany) in 2006 under Prof. Klaus Mullen. He finished his postdoctoral training in 2009 at the University of California Santa Barbara with Prof. Fred Wudl. In March 2009, he joined the Ulsan National Institute of Science and Technology (UNIST), Korea. He serves on the editorial board for Polymer (Korea) and works as a full-time professor at UNIST. His research focus is on the development of organic semiconducting materials and multifunctional molecule-related self-assembly for various applications, including organic solar cells, organic optoelectronics, triboelectric generations, and secondary batteries.

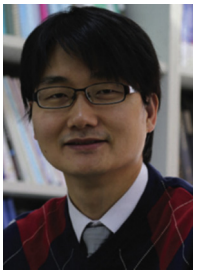

Tae-Woo Lee is a professor in Materials Science and Engineering at Seoul National University, Korea. He received his Ph.D in Chemical Engineering from KAIST, Korea in 2002. He joined Bell Laboratories, USA as a postdoctoral researcher and worked in Samsung Advanced Institute of Technology as a member of the research staff (2003–2008). He was an associate professor in Materials Science and Engineering at Pohang University of Science and Technology (POSTECH), Korea until Aug 2016. His research focuses on printed flexible electronics based on organic and organic-inorganic hybrid materials for flexible displays, nerve-inspired artificial electronic devices, solid-state lightings, and solar-energy-conversion devices.